ANALYSIS OF INSAR SENSITIVITY TO FOREST STRUCTURE BASED ON RADAR SCATTERING MODEL

D. W. Liu [†] and Y. Du

The Electromagnetics Academy
Zhejiang University
Hangzhou, 310058, China

G. Q. Sun

Department of Geography
University of Maryland
College Park, MD 20742 USA

W. Z. Yan

The Electromagnetics Academy
Zhejiang University
Hangzhou, 310058, China

B.-I. Wu

Department of Electrical Engineering and Computer Science
Massachusetts Institute of Technology
Cambridge, MA 02139, USA

Abstract—To investigate the effect of forest spatial structure on SAR interferometry (InSAR) data requires an electromagnetic scattering model capable of expressing radar observation in terms of parameters describing forest spatial structure. In this paper, we propose an electromagnetic scattering model for mixed-species forest which includes the coherent effect of forest structure and preserves phase information of radar backscattering signal. Interferometric SAR images of three-dimensional (3-D) scenes are simulated based on this model and the heights of scattering phase centers are estimated from the simulated InSAR data. The results show that the model is suitable

[†] Also with State Key Laboratory of Remote Sensing, Institute of Remote Sensing Applications, Chinese Academy of Sciences, P.O. Box 9718, Beijing, 100101, China.

for simulating interferometric SAR response to forest canopies and for investigating the forest spatial structure.

We also compare the backscattering coefficients predicted by the proposed electromagnetic scattering model with the JERS-1 L-band SAR and ENVISAT ASAR C-band data acquired at forest stands of Changqing test site in Daxinganling, Northern China. Good agreements are obtained between the model results and measurement data.

1. INTRODUCTION

Forest spatial structure, including tree height, biomass, vertical and horizontal heterogeneity, is an important factor influencing the exchanges of matter and energy between the landscape and atmosphere, and the biodiversity of ecosystems [1, 2]. Microwave remote sensing has been an important tool for detection of the structure of forest, especially SAR interferometry [3–7]. Radar backscattering signature, including the phase information in interferometric radar data, is dependent on the spatial structure of forest canopies. However it presents a big challenge to estimate the forest structure from InSAR data. Usually many important issues need to be considered in this estimation, but first of all, a high fidelity electromagnetic scattering model relating the InSAR data with the spatial structure properties of forest should be established. In order to improve the extraction of forest structure from InSAR data, many models are developed over the past decade [8–12]. In all these developed scattering models, the phase information in the backscattering signals is considered. For example, an interferometric SAR forest model based on "water-cloud model" was developed to provide complementary information to the information on coherence and effective interferometric tree height [8]. A physical model regarding forest canopies as either randomly or deterministically oriented volume is used to express the cross correlation applicable to interferometry, polarimetry, and polarimetric interferometry in terms of the parameters describing the vertical structure of vegetated land surfaces [9]. Recently some scattering models are developed including the coherent effect caused by the forest structure. For example, a Monte Carlo coherent scattering model for forest canopies using fractal-generated trees is used to simulate the interferometric SAR response for characterizing the scattering phase center statistics of forest canopies [10, 11]. And the descriptive coherent scattering model (COSMO), developed by Thirion et al. [12], is used to investigate attenuation, scattering phase center, and total height using simulated interferometric SAR

images of forested areas.

Although these models are capable of predicting SAR interferometric response of forest canopy, the 3-D spatial structure of forest canopies has not been adequately addressed in the above models. Important structural parameters, such as different ages and heights of trees, inter-tree gaps, and heterogeneous distributions of plant components (leaves and branches), have not been fully considered in above models.

In this paper, we propose an electromagnetic scattering model for simulation of interferometric SAR response from mixed-species forest canopies with complicated spatial structure. By this proposed model, we will investigate the effect of different structure of forest canopies on InSAR data. Finally the predicted backscattering coefficient by this model is compared with real SAR data of test site.

2. MODEL DESCRIPTION

The forest canopies are considered as a medium consisting of a great number of dielectric circular cylinders of finite size (stem, branches and needles) and thin dielectric disk (leaves). The total backscattering field of a radar image pixel is the coherent addition of scattering from all scatterers within the pixel. So the electromagnetic scattering model proposed in this paper requires information of the locations and orientations of these dielectric bodies in a forest stand. To build such a scene for a forest stand, the position, size, species and crown structure of every tree in the stand need to be specified. Some of these parameters, such as tree position, size and species, may be obtained from field measurement, but it is not practical to get the position of branches and leaves within the tree crowns. To circumvent this difficulty we resort to the L-system based on fractal theory, which allows realistic visualization of plant structures [13] given the geometric features of real plants. OpenGL is used to visualize tree architecture in order to tune the L-system for generating desired structure. In view of the fact that tree growth is determined not only by its gene type but also by its surrounding environment, a parametric L-system is used in this paper to describe the 3-D faithful tree architecture.

2.1. Main Scattering Mechanisms

The scattering mechanisms for forest canopy are decomposed into four major components: 1) direct backscattering from the scatterer as shown in Fig. 1(a); 2) scattering from the scatterer towards ground and then reflected from the ground to receiver as shown in Fig. 1(b);
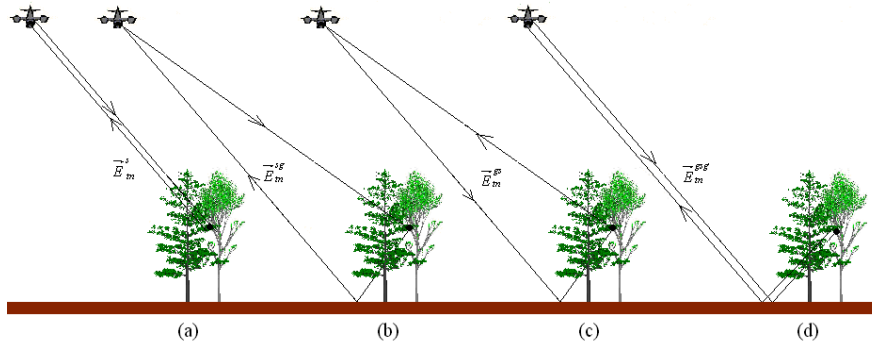
Figure 1. The major mechanisms for forest canopy.

2) scattering from the ground towards to the scatterer and then further scattered from the scatterer as shown in Fig. 1(c); and 4) multiple scattering with a path of ground-scatterer-ground as shown in Fig. 1(d).

2.1.1. Direct Backscattering from the Scatterer

For simplicity we model leaves as circular thin dielectric disks, because it was found through numerical simulation that unless ellipticity ratio is much larger than unity, the final backscatter is insensitive to the ellipticity ratio [14]. The radar scattering signals from leaves and thin branches are calculated using the generalized Rayleigh-Gans (GRG) approximation [15–17]. The trunk and relatively thick branches are calculated using method of infinite cylinder approximation [18–20].

An important issue in modeling the scattering from conifer is the scattering of needles. In such case, the near-field multiple scattering among needles cluster is expected to be strong [21, 22]. To include the effect of scattering interaction among needles, the approximate solution of the scattered field up to second order from two adjacent needles is presented. But in order to keep the computation tractable, we will mainly consider the second-order multiple scattering among needles in a single cluster (the needles around a twig) while ignoring the inter-cluster interaction. However, for leaves in a deciduous tree, because of the moderate number of leaves (relatively sparse), the near-field multiple scattering among leaves is ignored. So the forest canopies can be considered as a medium consisting of a great number of clusters of needles, dielectric cylinders of finite size (stem and branches), thin dielectric disks (leaves). That is, effectively we can consider a cluster of needles as a compound scatterer. In the following, we will present

the scattering from a cluster of needle.

We start with the standard assumption that there are two objects (O1 and O2) in free space. In the absence of O2, the scattered field $\overline{E}_1(\overline{r})$ from O1 illuminated by the incident field $\overline{E}_0^i$ is given by

$$\overline{E}_1(\overline{r}) = \frac{1}{4\pi} \left\{ \int_{v_1} \overline{\overline{G}}(\overline{r}, \overline{r}') e^{ik_0(\hat{k}_i \cdot \overline{r}' + R)} dv' \right\} \cdot \left(\overline{\overline{P}}_1 \cdot \overline{E}_0^i \right) \qquad (1)$$

where the primed coordinate represents the source, the unprimed coordinate represents the observation point. $\overline{r}$ and $\overline{r}'$ denote the position of observation point and the source O1, respectively. v_1 and v_2 are the volume of O1 and O2, respectively, and $R = |\overline{r} - \overline{r}'|$. Let $\hat{R} = $ unit vector from $\overline{r}$ to $\overline{r}'$

$$\overline{\overline{G}}(\overline{r}, \overline{r}') = \left(\frac{-1 + ik_0 R + k_0^2 R^2}{R^3} \right) \overline{\overline{I}} + \left(\frac{3 - 3ik_0 R - k_0^2 R^2}{R^3} \right) \hat{R}\hat{R} \quad (2)$$

Here the internal field is assumed to be able to be calculated using the Rayleigh approximation. So the polarization currents can be expressed in terms of the incident field and the polarization tensor [18], and $\overline{\overline{P}}_1$ is the polarizability tensor of O1. For O2, the polarization current excited by $\overline{E}_1$ can be written as $\overline{J}_2(\overline{r}'') = -ik_0 Y_0 \overline{\overline{P}}_2 \cdot \overline{E}_1 = -\frac{ik_0 Y_0}{4\pi} \overline{\overline{P}}_2 \left\{ \int_{v_1} \overline{\overline{G}}(\overline{r}, \overline{r}') e^{ik_0(\hat{k}_i \cdot \overline{r}' + R)} dv' \right\} \cdot (\overline{\overline{P}}_1 \cdot \overline{E}_0^i)$, where Y_0 is characteristic admittance of free space. Correspondingly, the second-order scattered field can be written as:

$$\overline{E}_{12}^s = -\frac{ik_0 z_0}{4\pi} \frac{e^{ik_0 r}}{r} \hat{k}_s \times \left\{ \hat{k}_s \times \int_{v_2} \overline{J}_2(\overline{r}'') e^{-ik_0 \hat{k}_i \cdot \overline{r}''} dv'' \right\} \qquad (3)$$

where z_0 is characteristic impedance of free space. The scattering matrix of these two needles can be expressed by:

$$S_{pq}^{12} = \left(\frac{k_0}{4\pi} \right)^2 \left(\overline{\overline{P}}_2 \cdot \hat{p} \right) \left\{ \int_{v_1} \int_{v_2} \overline{\overline{G}}(\overline{r}, \overline{r}') e^{ik_0(\hat{k}_i \cdot \overline{r}' - \hat{k}_s \cdot \overline{r}'' + R)} dv' dv'' \right\} \cdot \left(\overline{\overline{P}}_1 \cdot \hat{q} \right)$$
$$(4)$$

where $\hat{p}$ and $\hat{q}$ denote the scattering and incident polarization. $\overline{\overline{P}}$ is the polarizability tensor of O2. $\hat{k}_i$ and $\hat{k}_s$ denote the direction of the incident and scattering field, respectively. k_0 is the wave number in free space. r is the distance between O2 and receiving antenna. The

scattering from this compound scatterer (a cluster of needles) is the summation of first-order or second-order scattering amplitudes of the needles within this cluster as

$$\overline{\overline{S}}_{pq}^{n} = e^{ik_0(\hat{k}_i-\hat{k}_s)\cdot\overline{r}_n}$$

$$\left\{\sum_{i=1}^{N_n}e^{ik_0(\hat{k}_i-\hat{k}_s)\cdot\overline{r}'_i}\overline{\overline{S}}i_{pq}^{1st}+\sum_{i=1}^{N_n}\sum_{\substack{j=1\\j\neq i}}^{N_n}e^{ik_0(\hat{k}_i-\hat{k}_{ij})\cdot\overline{r}'_i}e^{ik_0\left|\overline{r}'_i-\overline{r}'_j\right|}e^{ik_0(\hat{k}_{ij}-\hat{k}_s)\cdot\overline{r}'_j}\overline{\overline{S}}ij_{pq}^{2nd}\right\}$$

$$(5)$$

where $\overline{\overline{S}}_{pq}^{n}$ denotes the scattering from the nth cluster. $\overline{\overline{S}}i_{pq}^{1st}$ and $\overline{\overline{S}}ij_{pq}^{2nd}$ are first-order or second-order scattering amplitudes of the needles in the nth cluster. N_n denotes the number of needles in the nth cluster. $\overline{r}_n$ is the position of the nth cluster in global coordinate system. $\overline{r}'_i$ and $\overline{r}'_j$ are the positions of the ith and jth needle in local coordinate system.

This approach is similar to the reciprocal approach developed by Sarabandi et al. [23]. Because the number of clusters in conifer is considerable, the computation of every cluster scattering involved in the calculation of first-order or second-order scattering of needles is very time consuming. To mitigate the computational complexity, the azimuth (from 0 to 2π) and zenith angle (from 0 to $\pi/2$) representing the orientation direction of a single cluster is discretized into a finite number. A look up table of scattering matrices for this finite number of orientation direction is generated for three principal scattering components: backscattering, forward scattering and bistatic scattering.

2.1.2. Scattering between Scatterer and Ground Surface

The ground bounce scattering between scatterer and ground surface often contributes significantly to overall backscattering. As such, it requires a good characterization of specular scattering from the ground surface [14]. Usually Fresnel reflection coefficient was directly used in recent scattering model for InSAR simulation where the ground surface was assumed to be specular (e.g., [10]), or a multiplicative attenuating factor $\exp[-2(k\sigma\cos\theta)^2]$ was added to account for the coherent reduction caused by surface height roughness (e.g., [24]). In this paper the modified Fresnel reflection coefficient developed by Rodriguez is used to evaluate the reflection coefficient of ground surface

[25].

$$\overline{\overline{R}}' = \overline{\overline{R}}_{Frensnel} \cdot \exp\left[-2(\sigma p_0)^2 \left(1 + \frac{\Gamma(0)}{2p_0^2}\right)^2\right] v \qquad (6)$$

where $\overline{\overline{R}}_{Frensnel}$ is the Fresnel reflection coefficient for a specular plane, $p_0 = k\cos\theta_i$ and $\Gamma(0)$ is the curvature. For a Gaussian correlated rough surface,

$$\Gamma(0) = \frac{C^{(2)}(0)}{L^2}\left(1 + \frac{1}{\cos^2\theta_i}\right) \qquad (7)$$

which denotes the second derivative of correlation function, where L is a length characteristic of the surface spectrum and $C^{(2)}(0)$ is the second derivative of the correlation function. From this method we can see that a curvature related term is analytically added to the multiplicative attenuating factor, resulting in an increase of the coherency as compared with otherwise.

2.2. Wave Propagation and Absorption in the Canopy

In order to determine accurately the absorption and scattering effects caused by forest canopy, the forest canopies are divided into small cubes. The Foldy's approximation is employed to evaluate the transmissivity matrix of each cube [26] and is briefly described as follows.

Transmissivity matrix of the mth cell can be denoted as:

$$\overline{\overline{T}}_m^u(L_m) = \begin{bmatrix} e^{i\overline{\overline{M}}_{hh,m}^u L_m} & 0 \\ 0 & e^{i\overline{\overline{M}}_{vv,m}^u L_m} \end{bmatrix} \qquad (8)$$

where u denotes the direction of incidence or reflection. L_m is the traveling length of radar wave in the mth cell. $\overline{\overline{M}}_m^u$ can be calculated by

$$\overline{\overline{M}}_m^u = \frac{2\pi}{k_0 d_m A_m} \sum_{n=1}^{N_m} \overline{\overline{F}}_n^0(\theta_u, \phi_u; \theta_u, \phi_u) \qquad (9)$$

where A_m is the surface area of the bottom side of the mth cell. d_m is the height of the mth cell. So the product $d_m A_m$ is the volume of the cell. N_m is the number of scatterers in the mth cell. $\overline{\overline{F}}_n^0(\theta_u, \phi_u; \theta_u, \phi_u)$ denotes the forward scattering matrix of the nth scatterer in the mth cell along the wave propagation directions.

If M cells are passed when radar beam travels from canopy top to the mth cell, from which the scattering from nth scatterer is to be

calculated, the transmissivity of the path from radar to the scatterer can be expressed as:

$$\overline{\overline{T}}_n^i = \overline{\overline{T}}_m^i \left(L_{mn}^i \right) \prod_{k=1}^{k=M} \overline{\overline{T}}_k^i \left(L_k^i \right) \tag{10}$$

where L_k^i is the pass length of radar wave in kth cell, and L_{mn}^i is the path length from the nth scatterer to the top of the mth cell. Similarly, $\overline{\overline{T}}_n^r$ and $\overline{\overline{T}}^t$ can be calculated similarly:

$$\overline{\overline{T}}_n^r = \overline{\overline{T}}_m^r \left(L_{mn}^r \right) \prod_{k=1}^{k=M_r} \overline{\overline{T}}_k^r \left(L_k^r \right) \tag{11}$$

$$\overline{\overline{T}}^t = \prod_{k=1}^{k=M_g} \overline{\overline{T}}_k^i \left(L_k^i \right) \tag{12}$$

where M_r is the number of cells passed by radar wave from the nth scatterer to ground, and M_g is the number of cells passed by radar wave in the path from ground back to radar.

In this study, a ray tracing method is used to calculate the path lengths of every cell when the radar beam travel through the forest canopy. Fig. 2 shows an example of the path length from L_1 to L_5 in every cell.

2.3. Scattering from a Forest Stands

The scattering matrices of all scatterers within a pixel are coherently added to give the total backscattering field. In this way the phase information of backscattering is preserved. Backscattering signal is mapped into a pixel according to its range or signal time delay.

2.4. Simulation of InSAR Data and Height Retrieval of Scattering Phase Center

In order to simulate the InSAR data (phase difference), the proposed scattering model is used to simulate the fields ($\overline{E}_1$ and $\overline{E}_2$) received by the antenna A1 and A2. Fig. 3 shows the configuration of InSAR geometry. So the phase difference between the signals collected by two antennae can be expressed as $\Delta\phi = \angle(\overline{E}_1^* \cdot \overline{E}_2)$.

The height of scattering phase center can be calculated from the following equations [27]
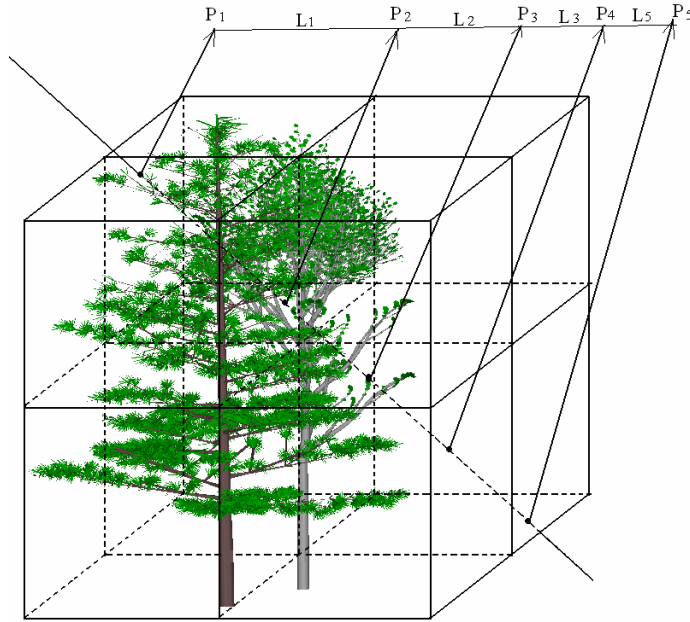
$$\delta = \frac{\lambda \Delta\phi}{2\pi} \tag{13}$$

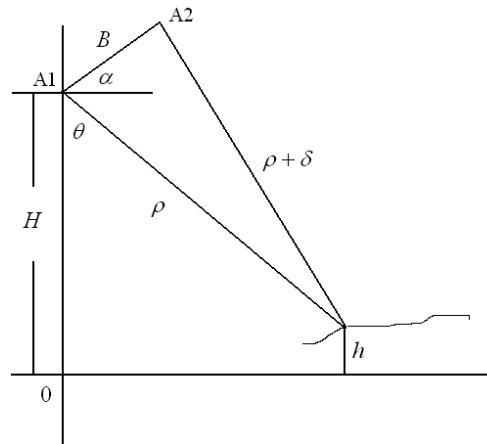**Figure 2.** The path length within every cell.

Figure 3. The configuration of InSAR geometry.

$$\sin(\alpha - \theta) = \frac{(\rho + \delta)^2 - \rho^2 - B^2}{2 \cdot \rho \cdot B} \approx \frac{\delta}{B} \tag{14}$$

$$h = H - \rho\cos\theta = H - \rho[\cos\alpha\cos(\alpha - \theta) + \sin\alpha\sin(\alpha - \theta)] \tag{15}$$

where δ denotes the path length difference relative to phase difference $\Delta\phi$. λ is the wavelength of incident field. ρ denotes the distance between antenna A1 and the scatterer. H is the altitude of antenna A1. B is the baseline length between antennae A1 and A2. θ and α are the radar incidence angle and the tilt angle of baseline with respect to the horizontal direction, respectively. From (15), the height of scattering phase center can be obtained. In the following simulations, we will mainly concentrate on characterizing the relationship between the height of scattering phase center and forest attributes.

3. MODEL SIMULATION AND EVALUATION

3.1. The Configuration of Forest Stand

To study the effect of forest canopy structure on the InSAR data requires the 3-D structure of forest stands as realistic as possible. We choose to use L-systems due to its recognized capability in this regard. The forest stands are established within a scene of 25 m along range by 10 m along azimuth. The tree positions on the ground surface are shown in Fig. 4. The total number of trees in the forest stand is 36.
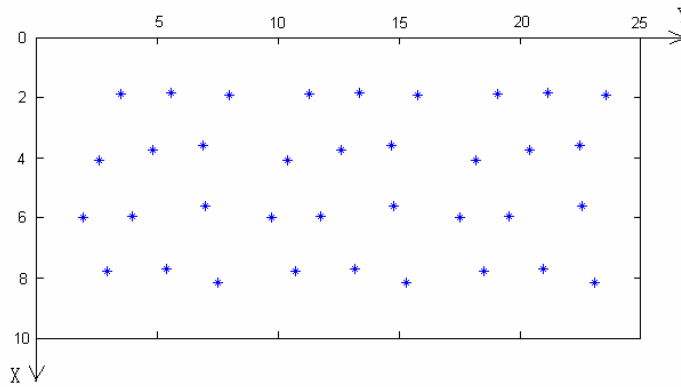

Figure 4. The position of the trees in every forest scene.

Table 1 and Table 2 list the structural parameters and dielectric constants of deciduous tree and conifer, respectively, where five different tree heights are considered, ranging from 5, 7.5, 10, 12.5 to 16 m. Accordingly, five scenes for different tree species are established based on L-systems. Figs. 5, 6 and 7 show the 3D structure of birch stand, larch stand and mix species stand (birch and larch), respectively, where the height is 16 m. One should note the distinctive structure of each tree despite the identical height in the stand.

Table 1. Deciduous tree.

Height of tree (m)		5	7.5	10	12.5	15
leaf	Radius (cm)	3.5	3.5	3.5	3.5	3.5
	Thickness (mm)	0.15	0.15	0.15	0.15	0.15
	Dielectric constant (L-band)	24.28+i7.91	24.28+i7.91	24.28+i7.91	24.28+i7.91	24.28+i7.91
	Density (N/m3)	340	280	210	270	300
Branch	Dielectric constant (L-band)	15.33+5.26i	15.33+5.26i	15.33+5.26i	15.33+5.26i	15.33+5.26i
	Density (N/m3)	80	50	17	12	7
Trunk	Average DBH (cm)	5.0	8.0	11.0	14.0	16.0
Crown	average height (m)	3.0	4.0	5.5	6.5	7.6
	average Width (m)	2.0	3.0	3.5	4.0	4.5

Table 2. Conifer.

| Height of tree (m)		5	7.5	10	12.5	15
needles	Radius (cm)	0.03	0.03	0.03	0.03	0.03
	Length (cm)	3	3	3	3	3
	Dielectric constant (L-band)	21.88+i7.22	21.88+i7.22	21.88+i7.22	21.88+i7.22	21.88+i7.22
	Density (N/m3)	72000	90000	120000	180000	240000
Branch	Dielectric constant (L-band)	15.33+5.26i	15.33+5.26i	15.33+5.26i	15.33+5.26i	15.33+5.26i
	Density (N/m3)	200	100	70	35	15
Trunk	Average DBH (cm)	4.0	6.0	9.0	12.0	14.1
Crown	Average height (m)	3.5	4.5	6.5	7.5	9.6
	Average Width (m)	0.9	1.5	3.0	4.0	4.5
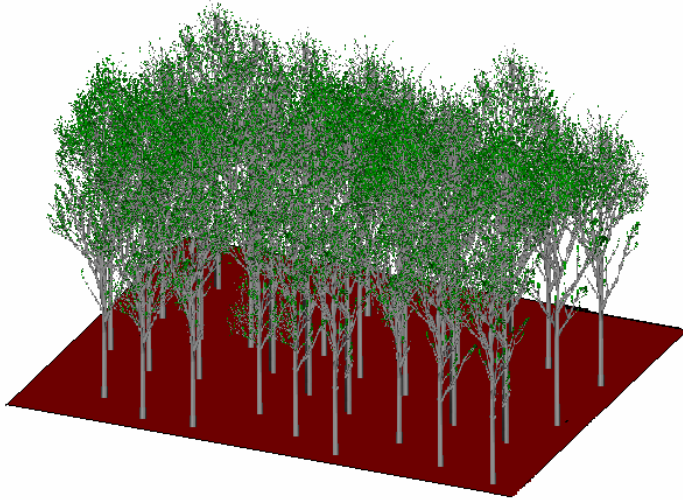
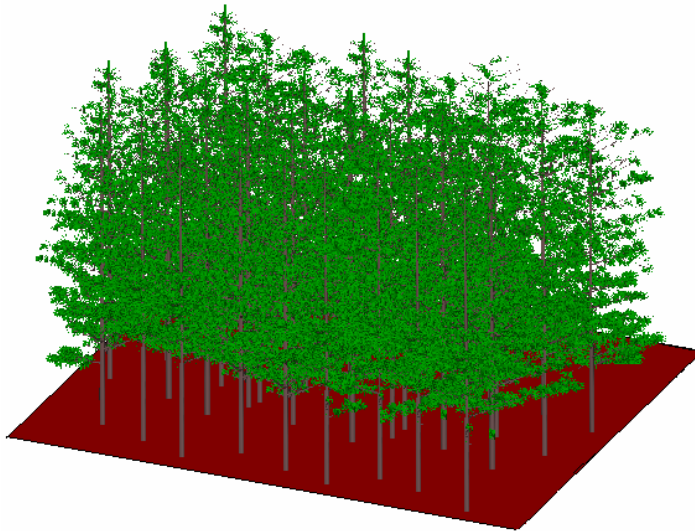**Figure 5.** Forest stand with only deciduous trees.

Figure 6. Forest stand with only conifer.

3.2. Model Simulation

In this study, we mainly concentrate on the simulation of InSAR data of the single-pass SAR interferometry mode. The radar system
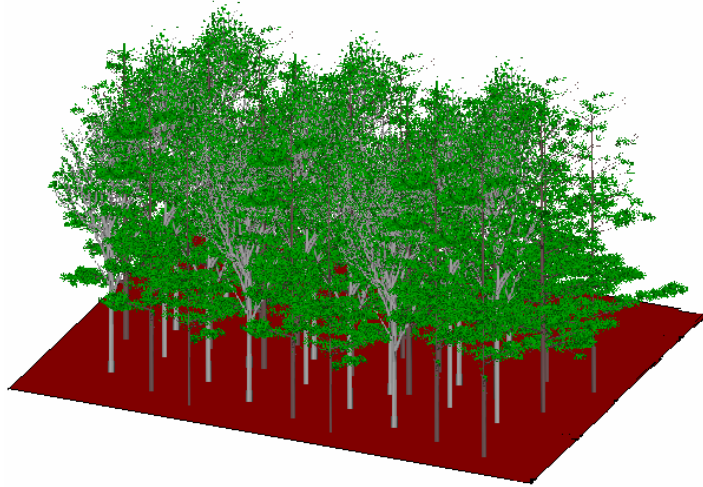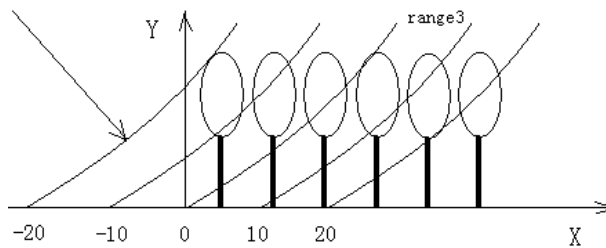
Figure 7. Mix species forest stand.

Figure 8. The simulation sketch of range.

parameters used in simulation are shown in Table 3. The above forest stands are taken as inputs to the radar coherent backscatter model and the InSAR signatures from entire stands are simulated. The heights of the phase centers in range (Fig. 8) are calculated from the simulated InSAR data (phase difference).

Figs. 9, 10 and 11 show the simulated height of scattering phase center versus the true height of forest stand of birch, larch and mix species at L-band for HH and VV polarizations, respectively. From these figures, it can be seen that the simulated height of the phase center increases as the true height of tree increases. This is expected because with increasing tree height, the tree is getting denser, so the extinction of canopy also increases. As a result, the direct backscattering components of scatterers increase, while contributions from ground-bounce and ground-scatter-ground scattering components
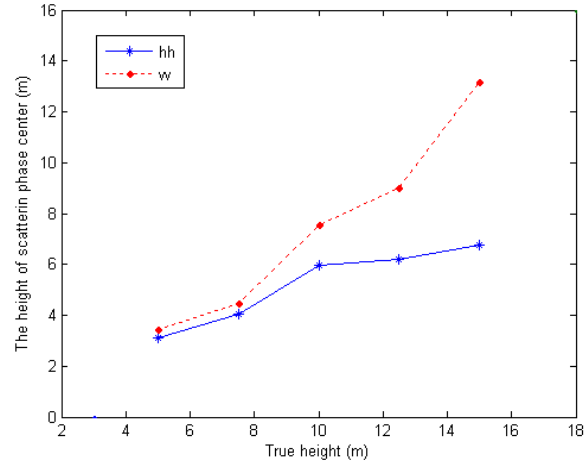
Figure 9. The height of scattering phase center versus the true height of forest stand with only deciduous tree.
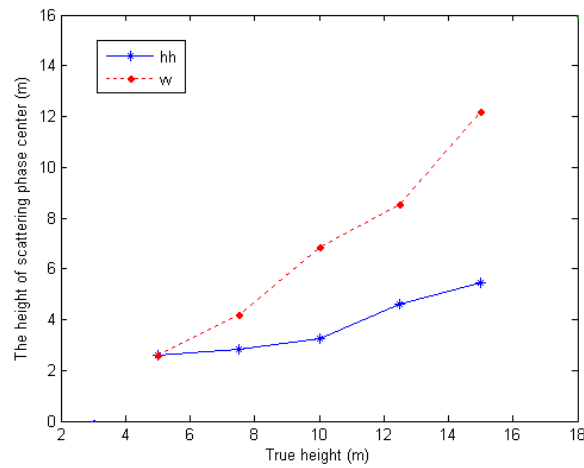

Figure 10. The height of scattering phase center versus the true height of forest stand with only conifer.

decrease, which results in an increase in the simulated height of phase center. From the figures, it is also observed that the simulated height of scattering phase center at VV polarization is always higher than that at HH polarization. There are mainly two reasons behind this phenomenon. One reason is that the specular scattering of ground surface at VV polarization is weaker than that at HH polarization,
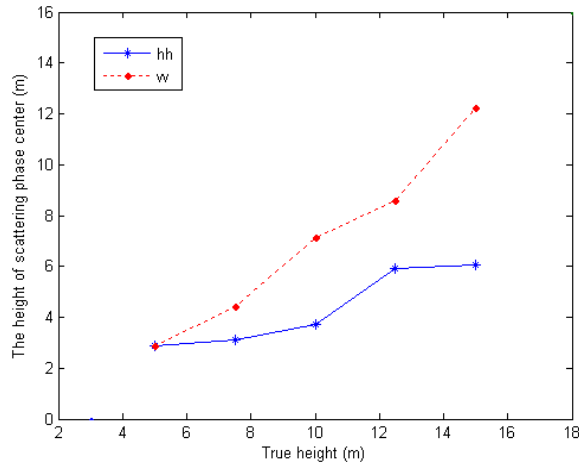
Figure 11. The height of scattering phase center versus the true height of forest stand with mix species.
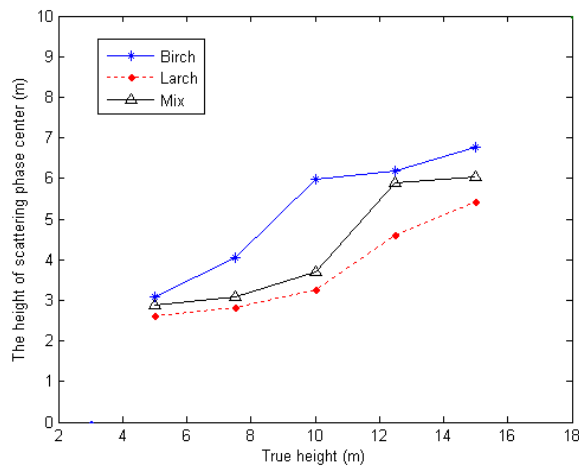
Figure 12. The comparison of height of scattering phase center among three tree species at HH polarization.

and the Fresnel reflection coefficient at VV polarization is positive (at least for the dominant real part) before the incidence angle reaches the Brewster angle, whereas that at HH polarization is negative, so at HH polarization the ground bounce scattering components become more dominant. The other reason is that the attenuation at the

VV polarization is higher than that at HH polarization, so at VV polarization, the ground bounce scattering contribution is weaker.

Fig. 12 and Fig. 13 show the effect of tree species on InSAR signal, where birch, larch and mixed species are considered. Among these three species, we can see that the simulated height of scattering phase center of deciduous forest is highest, while that of conifer forest is lowest. To see why this is the case, we need to examine the specific structures of these species. Fig. 14 shows the spatial structure of deciduous tree and conifer of the same height. We observe that leaves of deciduous tree are denser than those of conifer, and there are more scatterers near the top in deciduous tree than those in conifer. As a result, the forest canopy with only deciduous trees induces much stronger attenuation than other two tree species, and the relative
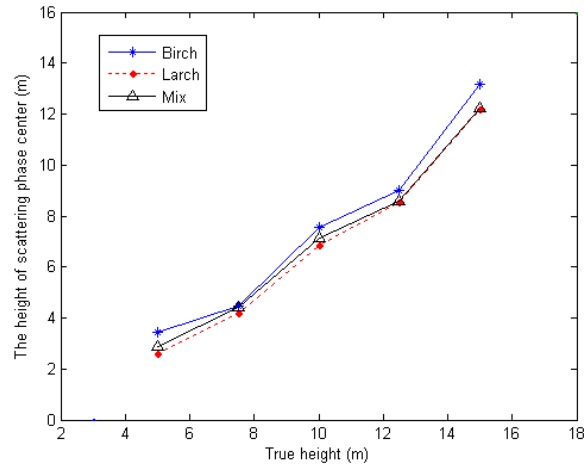

Figure 13. The comparison of height of scattering phase center among three tree species at VV polarization.

Figure 14. The spatial structure of deciduous tree and conifer.

Table 3. Radar system parameters.

Parameters	Value
Antenna Baseline (m)	2.58
Baseline Angle (deg)	62.77
Wavelength (L-band) (cm)	23.5
Wavelength (C-band) (cm)	5.6
Radar Height (m)	8500
Incidence Angle (deg)	35
Ground range resolution (m)	10
Azimuth resolution (m)	10

contributions from ground bounces to direct backscattering become weaker. Moreover, from Fig. 12 and Fig. 13, we also observe that this phenomenon is more obvious at HH polarization than at VV polarization, thanks to the higher attenuation at VV polarization than at HH polarization.

3.3. Simulation of Total Backscattering Intensity

In order to verify the scattering model, we also use it to predict the total backscattering intensity from a real radar pixel and compare with measurement data. The test site is in Changqing Forestry Bureau of Daxinanling forest in northeast China, near Amur River, centered approximately at 53°N and 123°E. The climate is cold, humid, and continental with intermediate annual precipitation. The three major tree species in the region are Dahurian Larch (*Larix gmelii*), Mongolian pine (*Pinus sylvestris var. mongolia*), and Asian White Birch (*Betula platyphylla*). Pure birch stands with various ages were located from the forest inventory map of Changqing as test sites in this study. The SAR data (JERS-1 SAR of 1997 and Envisat ASAR of 2003) of these stands were used to validate the results of the scattering model. Forest attributes (age, the number of tree, average DBH — diameter at breast height and height) of test stands within the Changqing forest were acquired through forest survey in 1999. Stand ages were adjusted by the time differences between the forest survey and radar data acquisitions.

Measured parameters of pure birch trees of test site are shown

Table 4. Measured ground truth parameters.

| Age	DBH (m)	Height (m)	Crown height (m)	Crown width (m)	Leaf density (No./m^3)	Branch density (No./m^3)	Plant density (No./30*30m^2)	Thickness of leaf (mm)	Radius of leaf (cm)
10	3.0	4.57	2.1	0.9	340	75	533	0.15	2.5
30	10.0	10.8	4.9	2.1	210	15	189	0.15	4.5
40	12.5	13.9	6.1	3.5	310	11	120	0.15	4.5
50	14.1	15.6	7.6	4.0	340	7	68	0.15	4.5
60	14.1	15.6	7.6	4.0	196	5	28	0.15	4.5

Table 5. Dielectric properties of the tree components.

	L-band	C-band
Leaf	24.28+i7.91	20.24+i6.78
Branch	15.33+i5.26	12.30+i4.16
Soil	10.0+i2.0	9.6+i2.04

in Table 4 [28]. Table 5 shows the dielectric properties of the birch tree components and soil regardless of the age of tree. The root-mean-square (rms) height and correlation length of the surface are 0.015 m and 0.11 m, respectively. Based on these parameters, we are able to simulate the forest stands at 6 ages using L-system, which are then used as input to the scattering model.

Figs. 15(a) and (b) show the backscattering coefficients of birch stands versus the age of tree at L-band and C-band. From this figure, we observe that the predicted radar backscattering coefficients agree well with both JERS-1 L-band and ASAR C band data. From the age of 10 to 30, the backscattering coefficient drops down, while from the age of 30 to 50, it goes up gradually. After the age of 50, it descends again. It shows a growing cycle of birch tree. At the age of 10, the forest stand is very dense with numerous little trees, so the magnitude of the backscattering coefficient is appreciable. However with the tree growing (till the age of 30) competitively, the number of plant in the forest stand decreases dramatically. Although during the course of this growth, the tree becomes denser than before, the new products are less than the lost, so the backscattering coefficient still drops down. After the age of 30, the number of plant tends to stabilization. During this period of time, the new products are higher than the lost, so the
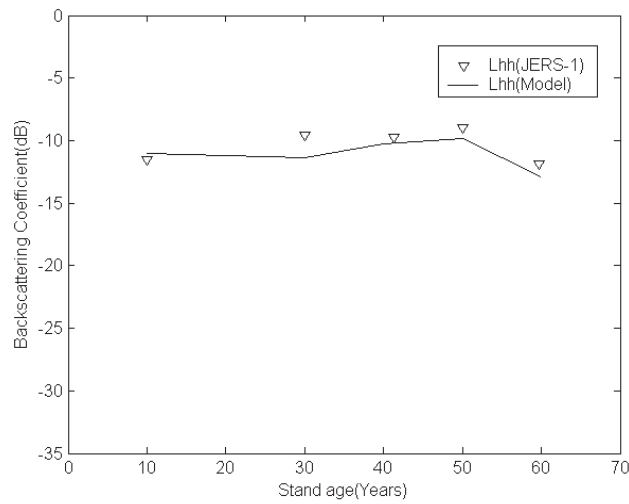
(a)
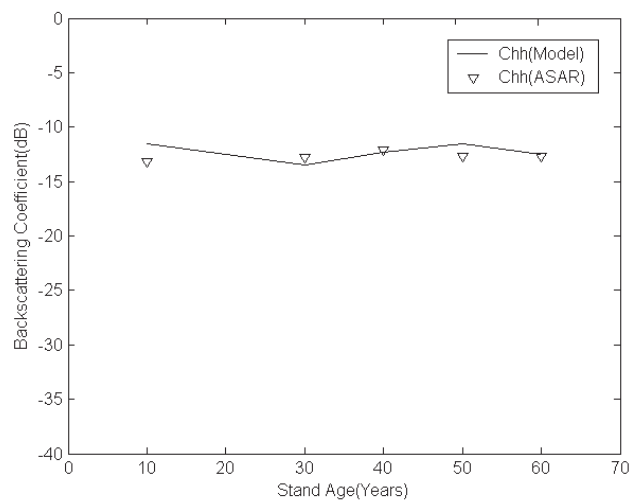
(b)

Figure 15. (a) Comparisons of simulation LHH backscatter with JERS-1 data from several stands, (b) Comparisons of simulation CHH backscatter with ENVISAT ASAR data from several stands.

backscattering coefficient of forest stand will ascend. However, from the age of 50, since the maximum age of birch tree is 60 in Changqing forest, many big trees are dying, while new trees are small. Hence the backscattering coefficient decreases very fast. In short, from this figure, we can see the growing cycle of birch tree vividly.

4. DISCUSSION AND CONCLUSION

In this paper, we have developed a three-dimensional coherent scattering model for mix-species forest based on realistic forest scene, and have simulated the backscattering intensity of birch forest stand. The results show a good agreement of backscattering coefficients between the model prediction and real radar data at L- and C-band. Because this model preserves the phase information, it is useful in interpreting interferometric SAR data. The simulated scattering phase center heights from different stand structures look reasonable, and provide valuable insights into the characteristics of InSAR data.

The spatial structure of forest stands has considerable impact on the height of scattering phase center (a product of InSAR data). As we can see from Figs. 12 and 13 that even when the forest stands have the same height and location of tree in forest stand, and the properties of ground are identical, the height of scattering phase center changes with the tree species. In the cases when a radar beam penetrates the canopy, the stronger the contributions from ground-bounce, the lower the location of the scattering phase center obtained from the phase difference of SAR interferometry. From the simulation results, we can see the proposed scattering model of mix-species forest can be used to investigate the effect of forest spatial structure on InSAR data.

Our next step is to focus on the development of inversion algorithm based on the proposed scattering model to retrieve important forest parameters such as density and tree types. Such inversion algorithm is expected to be helpful in forest dynamic studies and forest physical parameters estimation from InSAR data.

ACKNOWLEDGMENT

REFERENCES

1. Lefsky, M. A., W. B. Cohen, S. A. Acker, G. G. Parker, T. A. Spies, and D. Harding, "Lidar remote sensing of the canopy structure and biophysical properties of Douglas-fir western hemlock forests," *Remote Sensing of Environment*, Vol. 70, 339–361, 1999.

2. Yang, R. and M. Friedl, "Modeling the effects of three-dimensional vegetation structure on surface radiation and energy balance in boreal forests," *J. Geophysics. Research*, Vol. 108, 1–11, 2003.

3. Huang, E. X. and A. K. Fung, "Electromagnetic wave scattering from vegetation with odd-pinnate compound leaves," *J. of Electromagn. Waves and Appl.*, Vol. 19, 231–244, 2005.

4. Cho, B. L. and Y. S. Kim, "Multilook coherence estimation using adaptive weighted window in interferometric SAR," *J. of Electromagn. Waves and Appl.*, Vol. 21, No. 3, 359–365, 2007.

5. Lim, T. S., V. C. Koo, H. T. Ewe, and H. T. Chuah, "High-frequency phase error reduction in SAR using particle swarm of optimization algorithm," *J. of Electromagn. Waves and Appl.*, Vol. 21, No. 6, 795–810, 2007.

6. Soliman, M. S., T. Morimoto, and Z.-I. Kawasaki, "Three-dimensional localization system for impulsive noise sources using Ultra-wideband digital interferometer technique," *J. of Electromagn. Waves and Appl.*, Vol. 20, No. 4, 515–530, 2006.

7. Koo, V. C., Y. K. Chan, and H. T. Chuah, "Multiple phase difference method for real-time SAR autofocus," *J. of Electromagn. Waves and Appl.*, Vol. 20, No. 3, 375–388, 2006.

8. Askne, J. I. H., P. B. G. Dammert, L. M. H. Ulander, and G. Smith, "C-band repeat-pass interferometric SAR observations of the forest," *IEEE Trans. Geosci. Remote Sensing*, Vol. 35, 25–35, Jan. 1997.

9. Treuhaft, R. N. and P. R. Siqueira, "Vertical structure of vegetated land surfaces from interferometric and polarimetric radar," *Radio Sci.*, Vol. 35, 141–177, Jan. 2000.

10. Lin, Y. C. and K. Sarabandi, "A Monte Carlo coherent scattering model for forest canopies using fractal generated trees," *IEEE Trans. Geosci. Remote Sensing*, Vol. 37, 36–40, Jan. 1997.

11. Sarabandi, K. and Y. C. Lin, "Simulation of interferometric SAR response for characterizing the scattering phase center statistics of forest canopies," *IEEE Trans. Geosci. Remote Sensing*, Vol. 38, 115–125, Jan. 2000.

12. Thirion, L., E. Colin, and C. Dahon, "Capabilities of a forest

coherent scattering model applied to radiometry, interferometry, and polarimetry at P- and L-band," *IEEE Trans. Geosci. Remote Sensing*, Vol. 44, 849–862, Apr. 2006.

13. Prusinkiewicz, P. and A. Lindenmayer, *The Algorithmic Beauty of Plants*, Spring-Verlag, New York, 1990.

14. Du, Y., Y. L. Luo, W. Z. Yan, and J. A. Kong, "An electromagnetic scattering model for soybean canopy," *Progress In Electromagnetics Research*, PIER 79, 209–223, 2008.

15. Karam, M. A., A. K. Fung, and Y. M. M. Antar, "Electromagnetic wave scattering from some vegetation samples," *IEEE Trans. Geosci. Remote Sensing*, Vol. 26, 799–808, Nov. 1988.

16. Khatir, B. N., M. Al-Kanhal, and A. Sebak, "Electromagnetic wave scattering by elliptic chiral cylinder," *J. of Electromagn. Waves and Appl.*, Vol. 20, No. 10, 1377–1390, 2006.

17. Zhong, X. M., C. Liao, W. Chen, Z. B. Yang, Y. Liao, and F.-B. Meng, "Image reconstruction of arbitrary cross section conducting cylinder using UWB pulse," *J. of Electromagn. Waves and Appl.*, Vol. 21, No. 1, 25–34, 2007.

18. Sarabandi, K. and T. B. A. Senior, "Low-frequency scattering from cylindrical structures at oblique incidence," *IEEE Trans. Geosci. Remote Sensing*, Vol. 28, 879–885, Sep. 1990.

19. Ruppin, R., "Scattering of electromagnetic radiation by a perfect electromagnetic conductor cylinder," *J. of Electromagn. Waves and Appl.*, Vol. 20, No. 13, 1853–1860, 2006.

20. Vecchia, A. Della, L. Guerriero, I. Bruni, and P. Ferrazzoli, "Hollow cylinder microwave model for stems," *J. of Electromagn. Waves and Appl.*, Vol. 20, No. 3, 301–318, 2006.

21. Ferrara, F., C. Gennarelli, R. Guerriero, G. Riccio, and C. Savarese, "An efficient near-field to far-field transformation using the planar wide-mesh scanning," *J. of Electromagn. Waves and Appl.*, Vol. 21, No. 3, 341–357, 2007.

22. Ayestaran, R. G. and F. Las-Heras, "Near field to far field transformation using neural networks and source reconstruction," *J. of Electromagn. Waves and Appl.*, Vol. 20, No. 15, 2201–2213, 2006.

23. Sarabandi, K. and P. F. Polatin, "Electromagnetic scattering from two adjacent objects," *IEEE Trans. Antennas. Propagat.*, Vol. 42, 510–517, Apr. 1994.

24. Marliani, F., S. Paloscia, P. Pampaloni, and J. A. Kong, "Simulating coherent backscattering from crops during the growing cycle," *IEEE Trans. Geosci. Remote Sensing*, Vol. 40,

162–177, Jan. 2002.

25. Rodriguez, E., "Beyond the Kirchhoff approximation," *Radio Sci.*, Vol. 26, 121–132, 1991.

26. Tsang, L., J. A. Kong, and R. T. Shin, *Theory of Microwave Remote Sensing*, Wiley Interscience, New York, 1985.

27. Zebker, H. A., S. N. Madsen, J. Martin, K. B. Wheeler, T. Miller, Y. Lou, G. Alberti, S. Vetrella, and A. Cucci, "The TOPSAR interferometric radar topographic mapping instrument," *IEEE Trans. Geosci. Remote Sensing*, Vol. 30, No. 5, 1992.

28. Guo, Z., "Radar backscattering analysis for Boreal Taiga Forest and biomass inversion based on model," Ph.D. thesis, Institute of Remote Sensing Applications, Chinese Academy of Scienes, 2005.